

Supporting Information

Solvent-Mediated Purification of Hexa-Molybdenum Cluster Halide, Cs₂[Mo₆Cl₁₄] for Enhanced Optical Properties

*Norio Saito^{1,2,3}, Pierrick Lemoine⁴, Stéphane Cordier⁴, Yoshiki Wada^{2,5}, Takeo Ohsawa^{2,5}, Noriko Saito², Fabien Grasset^{2,3}, Jeffrey Scott Cross¹, Naoki Ohashi^{*2,3,5,6}*

¹ Department of Metallurgy and Ceramics Science, Tokyo Institute of Technology (Tokyo Tech.), 2-12-1 Ookayama, Meguro, Tokyo 152-8551, Japan.

² National Institute for Materials Science (NIMS), 1-1 Namiki, Tsukuba, Ibaraki 305-0044, Japan.

³ Laboratory for Innovative Key Materials and Structures (LINK; UMI 3629), National Institute for Materials Science, 1-1 Namiki, Tsukuba, Ibaraki 305-0044, Japan.

⁴ Institut des Sciences Chimiques de Rennes (ISCR; UMR 6226), University of Rennes 1, General Leclerc, Rennes 35042, France.

⁵ NIMS-Saint-Gobain Center of Excellence for Advanced Materials, NIMS, 1-1 Namiki, Tsukuba, Ibaraki 305-0044, Japan.

⁶ Materials Research Center for Element Strategy (MCES), Tokyo Institute of Technology, Midori-ku, Yokohama 226-0026, Japan.

* Corresponding author: OHASHI.Naoki@nims.go.jp

1. Materials and experimental methods

1.1 Preparation of $\text{Cs}_2[\text{Mo}_6\text{Cl}_{14}]$ and $\text{Cs}_2[\text{Mo}_6\text{Cl}_{14}]\cdot\text{H}_2\text{O}$ precursors

The trigonal $\text{Cs}_2[\text{Mo}_6\text{Cl}_{14}]$ precursor was prepared through a solid-state reaction and subsequent purification as described previously [1,2]. Before carrying out any recrystallization experiments, the precursor was heated at 150 °C in a glove box filled with dry N_2 gas (< 0.1 ppm H_2O) in order to remove residual water molecules.

The monoclinic $\text{Cs}_2[\text{Mo}_6\text{Cl}_{14}]\cdot\text{H}_2\text{O}$ precursor was prepared through ion exchange using $(\text{H}_3\text{O})_2[\text{Mo}_6\text{Cl}_{14}]\cdot 7\text{H}_2\text{O}$ as the starting material. First, $(\text{H}_3\text{O})_2[\text{Mo}_6\text{Cl}_{14}]\cdot 7\text{H}_2\text{O}$ (10 g, 8.10 mmol) was prepared following a literature procedure [3]. The hydrated-complex compound was then dissolved in ethanol (10 mL), and the resulting solution was heated to reflux. A solution was prepared by dissolving CsCl (2.75 g, 16.3 mmol) in ethanol (10 mL) by heating under reflux. The CsCl solution was subsequently added to the cluster solution, with stirring, in order to achieve the exchange of H_3O^+ for Cs^+ cations. After filtration, the obtained solid was purified by dissolution and filtration using acetone as the solvent. Finally, crystals of the $\text{Cs}_2[\text{Mo}_6\text{Cl}_{14}]\cdot\text{H}_2\text{O}$ precursor were obtained by rotary evaporation of the solvent at 25 °C under vacuum.

1.2 Ultraviolet-visible absorbance measurement for solubility determination

Ultraviolet-visible absorption spectra of the supernatant solutions collected from each suspension were measured using a SolidSpec-3700 spectrophotometer (Shimadzu). The concentration of $[\text{Mo}_6\text{Cl}_{14}]^{2-}$ was photospectroscopically determined by use of the standard curve method that correlates absorption spectral intensities with $[\text{Mo}_6\text{Cl}_{14}]^{2-}$ concentration. Figure S1 ensures linear relationship between absorbance value at 310 nm and $[\text{Mo}_6\text{Cl}_{14}]^{2-}$ concentration.

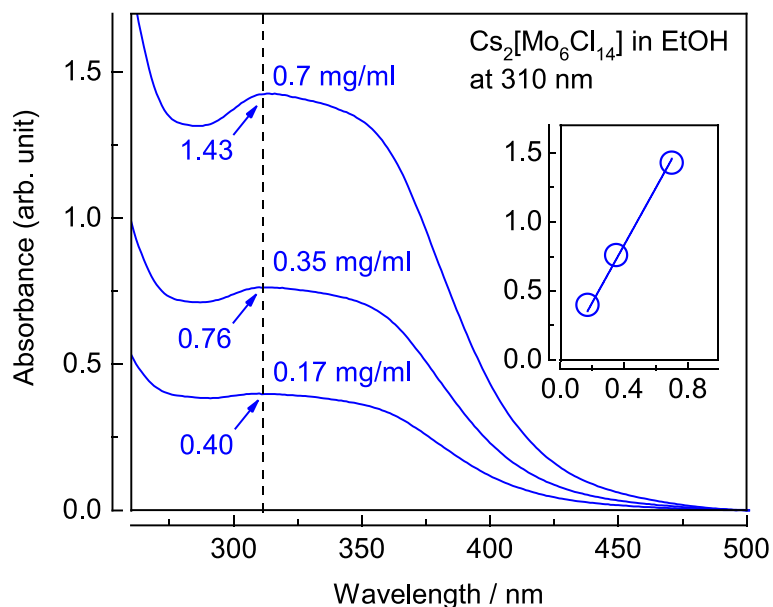


Figure S1 Absorption spectra of $[\text{Mo}_6\text{Cl}_{14}]^{2-}$ dissolved in EtOH solutions as a function of its concentration. The inset shows a standard curve obtained from linear relationship between observed absorption values at 310 nm and $[\text{Mo}_6\text{Cl}_{14}]^{2-}$ concentrations.

1.3 Powder X-ray diffraction (XRD)

Powder XRD patterns of the samples collected from the recrystallization experiments were measured using an Ultima III X-ray diffractometer (Rigaku) with $\text{CuK}\alpha$ radiation ($\lambda = 0.1540562$ nm). The lattice parameters of the identified phases were determined from the indexed XRD patterns using a least-squares method. Here, more than ten observed diffraction peaks were involved in the determination of lattice parameters of sufficiently high accuracy.

Phase identification by XRD patterns were performed by comparing measured profile and simulated profiles. Tables S1 and S2 shows reported structural parameters of $\text{Cs}_2[\text{Mo}_6\text{Cl}_{14}]$ and $\text{Cs}_2[\text{Mo}_6\text{Cl}_{14}] \cdot \text{H}_2\text{O}$ [1]. Simulation of XRD patterns was performed by using parameters shown in these tables. Those parameters were also used as initial structure for density functional theory (DFT) calculations.

Table S1 Structural parameters of Cs₂[Mo₆Cl₁₄] reported in a reference [1].

Compound		Cs ₂ [Mo ₆ Cl ₁₄]			
<i>Z</i>		2			
Crystal system; Space group		Trigonal; $P\bar{3}1c$			
Lattice parameters		$a = 0.9823$ nm; $c = 1.4197$ nm; $V = 1.1862$ nm ³			
Atom	Wyck.	Occ.	<i>x</i>	<i>y</i>	<i>z</i>
Cs1	2 <i>c</i>	1.0	1/3	2/3	0.2500
Cs2	4 <i>e</i>	0.5	0	0	0.0203
Mo	12 <i>i</i>	1.0	0.5138	0.3350	0.1751
Cl1	4 <i>f</i>	1.0	2/3	1/3	0.0390
Cl2	12 <i>i</i>	1.0	0.3752	0.0452	0.1770
Cl3	12 <i>i</i>	1.0	0.3085	0.3467	0.0855

Table S2 Experimentally determined structural parameters of Cs₂[Mo₆Cl₁₄]•H₂O [1].

Compound		Cs ₂ [Mo ₆ Cl ₁₄]•H ₂ O			
<i>Z</i>		4			
Crystal system; Space group		Monoclinic; <i>C2/c</i>			
Lattice parameters		<i>a</i> = 1.9564 nm; <i>b</i> = 1.5141 nm; <i>c</i> = 0.9340 nm; <i>β</i> = 115.63°; <i>V</i> = 2.4945 nm ³			
Atom	Wyck.	Occ.	<i>x</i>	<i>y</i>	<i>z</i>
Cs1	4 <i>a</i>	1.0	0	0	0
Cs2	4 <i>e</i>	1.0	0	0.4416	1/4
Mo1	8 <i>f</i>	1.0	0.2067	0.2700	0.1380
Mo2	8 <i>f</i>	1.0	0.2964	0.3584	0.0503
Mo3	8 <i>f</i>	1.0	0.3328	0.1992	0.1625
Cl1	8 <i>f</i>	1.0	0.3317	0.3235	0.3322
Cl2	8 <i>f</i>	1.0	0.1746	0.4208	0.0250
Cl3	8 <i>f</i>	1.0	0.4141	0.2864	0.0719
Cl4	8 <i>f</i>	1.0	0.2440	0.1184	0.2368
Cl5	8 <i>f</i>	1.0	0.1479	0.2961	0.3170
Cl6	8 <i>f</i>	1.0	0.3590	0.5015	0.1164
Cl7	8 <i>f</i>	1.0	0.4422	0.1304	0.3768
O	4 <i>e</i>	1.0	0	0.1550	1/4
H	8 <i>f</i>	1.0	0.032	0.187	0.272

1.4 Thermal desorption spectroscopy (TDS)

Thermal desorption spectra (TDS) were measured using an EMD-WA1000 analyzer (ESCO), equipped with an ultra-high-vacuum (UHV) chamber in which the background pressure was kept below 6.0×10^{-10} torr. The sample (1.0 mg), mounted on a SiC holder, was heated in the UHV chamber at a heating rate of 10 °C/min to obtain temperature-programed desorption spectra.

1.5 Fourier transform infrared spectroscopy (FTIR)

Fourier transform infrared spectroscopy (FT-IR) was also performed at room temperature using a Nicolet iS50 spectrometer (Thermo Scientific) with a diffuse reflectance setup. The collected precipitates were diluted by mixing with dried KBr powder in a weight ratio of sample:KBr of 1:20.

1.6 Luminescence (PL) and time-resolved luminescence (TRPL) spectroscopy

The luminescence of each cluster complex compound was excited with a pulsed laser (100 fs pulse width, 1 kHz repetition frequency) generated by an optical parametric amplifier (Spectra Physics TOPAS Prime) excited by a titanium sapphire regenerative (Ti-Sap) amplifier (Spectra Physics Solstice). The wavelength of the laser pulse was set to 410 nm. PL spectra were recorded with a VM-505 monochromator (Acton Research) and detected with an InGaAs photodiode. On the other hand, TRPL profiles were obtained with a SpectroPro-300i monochromator (Acton Research) and a C5680 streak camera equipped with a M5677 sweep unit (Hamamatsu Photonics).

2. Detail of DFT calculation

Electronic structures of $\text{Cs}_2[\text{Mo}_6\text{Cl}_{14}]$ and $\text{Cs}_2[\text{Mo}_6\text{Cl}_{14}]\cdot\text{H}_2\text{O}$ were simulated by plane-wave (PW) based DFT calculation. The calculation was performed on the basis of the method we recently reported in reference [4] and revised by considering the scalar relativistic treatment.

The CASTEP code [5] based on norm-conserving pseudo-potentials (NCPPs) [6–8] was utilized for all calculations. In the present study, NCPPs were generated considering the formalism of scalar relativistic treatment described in the literature [9], while the relativistic effects were not considered in our previous study [4]. Generalized gradient approximation (GGA) optimized for solid-state compounds, i.e., the PBEsol functional [10], was used as the exchange-correlation functional for total energy calculations. Density mixing and structural relaxation schemes were the same as those of the reference [4]. The PW cut-off energy was set to 990 eV and a Monkhorst-Pack grid [11,12] ($4 \times 4 \times 3$ mesh) was employed for Brillouin zone sampling. The convergence tolerances were set to 5×10^{-5} nm for atomic displacement, 5×10^{-6} eV/atom for total energy, 0.1 eV/nm for maximum interatomic force, and 0.02 GPa for pressure.

3. Results

3.1 Phase identification of prepared precursors

Figure S2 shows the observed XRD patterns of the prepared precursors. In this figure, simulated XRD patterns obtained using the reported structural parameters of the monoclinic (Fig. S2(a)) and trigonal (Fig. S2(f)) phases are also shown. The monoclinic-phase precursor was clearly obtained as a single phase, since the XRD pattern in Fig. S2(b) is in good agreement with the simulated pattern displayed in Fig. S2(a). On the other hand, the powder prepared with the aim of obtaining the trigonal phase contained significant amounts of the monoclinic phase as evidenced by comparing the observed (Fig. S2(d)) and simulated (Figs. S2(a) and S2(f)) patterns. Subsequent heat treatment at 150 °C was unable to induce complete transformation of the residual monoclinic phase to the trigonal phase, as shown in Fig. S2(e). This indicates that the complete removal of water from the cluster compound is very difficult. As this powder is dominated by the trigonal phase, with only a very minor amount of the residual monoclinic form present after heating at 150 °C under N₂ (see the very weak peak indicated by the arrow in Fig. S2(e)).

As previously reported, it is noteworthy that the monoclinic phase decomposed to the trigonal phase during storage [1]. The XRD pattern shown in Fig. S2(c) was obtained from a sample of the prepared monoclinic-phase powder that was kept for more than 4 weeks in a dry atmosphere; it is clear that the sample had evolved into the trigonal form, Cs₂[Mo₆Cl₁₄]. This indicates that the monoclinic phase, Cs₂[Mo₆Cl₁₄]•H₂O, is not very stable in a dry atmosphere. However, the complete decomposition of the monoclinic phase to pure Cs₂[Mo₆Cl₁₄] by thermal treatment was not successful, as evidenced by the XRD pattern shown in Fig. S2(e). Hence, these results are good examples that demonstrate the difficulty in dehydrating Cs₂[Mo₆Cl₁₄].

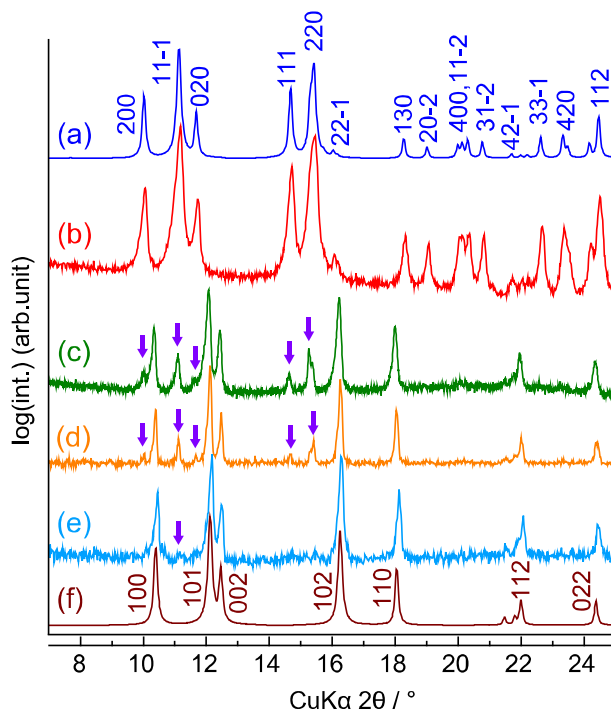


Figure S2 XRD patterns for the precursor compounds, (a) simulated for monoclinic $\text{Cs}_2[\text{Mo}_6\text{Cl}_{14}]\cdot\text{H}_2\text{O}$, (b) observed for synthesized $\text{Cs}_2[\text{Mo}_6\text{Cl}_{14}]\cdot\text{H}_2\text{O}$, (c) observed $\text{Cs}_2[\text{Mo}_6\text{Cl}_{14}]\cdot\text{H}_2\text{O}$ after storage for 4 weeks, (d) observed for as-prepared $\text{Cs}_2[\text{Mo}_6\text{Cl}_{14}]$, (e) observed for $\text{Cs}_2[\text{Mo}_6\text{Cl}_{14}]$ after heating at 150 °C in N_2 , (f) simulated for trigonal $\text{Cs}_2[\text{Mo}_6\text{Cl}_{14}]$. Arrows indicate peaks for the residual trigonal phase.

3.2 TDS spectra

The TDS profile of the trigonal-phase powder collected from 1-PrOH also exhibits three peaks, as shown in Fig. S3. However, this profile differs from that of the sample prepared using EtOH. The features found in Fig. S3(a), are the desorption peak for $m/z = 60$, which corresponds to the $^{12}\text{C}_3^1\text{H}_8^{16}\text{O}$ fragment, and that for $m/z = 12$, which corresponds to ^{12}C that are observed at different temperatures. In fact, the $m/z = 60$ peak is observed at 181 °C, while the $m/z = 12$ peak is observed at 235 °C. It should be noted that not all TDS profiles for the $^{12}\text{C}_n^1\text{H}_m$ and $^{12}\text{C}_n^1\text{H}_m^{16}\text{O}$ fragments are shown in this figure, but their TDS profiles exhibited peaks at different temperatures. For instance, the spectrum for $m/z = 15$,

corresponding to [$^{12}\text{C}^1\text{H}_3$], appears to have peaks at both 181 and 235 °C, while that for $m/z = 42$ exhibits a peak at 194 °C associated with a very broad tail in the high-temperature region. This behavior indicates that 1-PrOH ($\text{C}_3\text{H}_7\text{OH}$) molecules decompose at relatively high temperatures and that the decomposition behavior changes with sample temperature.

We next focus on the water-related fragment, i.e., the $m/z = 18$ peak in the TDS spectra of the sample prepared with 1-PrOH. A peak corresponding $m/z = 18$ was observed at 228 °C, which is very close to the temperature where the profile for $m/z = 12$ exhibits a peak. Because it is well known that an $m/z = 18$ fragment is formed during the molecular rearrangements of alcohols in mass spectrometry [13], it is difficult to distinguish whether the $m/z = 18$ desorption profile, i.e., [$^1\text{H}_2^{16}\text{O}$], is dominated by the desorption of water from the trigonal phase or the decomposition of the residual solvent. At the present time, we tentatively attribute the $m/z = 18$ TDS signal to fragments resulting from the decomposition of 1-PrOH, since the decomposition of 1-PrOH results in the desorption of a [^{12}C] fragment that must be associated with the desorption of hydrogen and oxygen-containing fragments. This means that the trigonal-phase powder collected from 1-PrOH does not show any trace of water desorption from its crystalline lattice, although the sample prepared with EtOH showed evidence of water desorption, as described in the main text

Figure S3(b) shows TDS profile for the sample recrystallized in MeOH suspension. Two significant peaks were found in the TDS profile for the sample prepared with MeOH; the peak at lower temperature, i.e., 103 °C, was observed in the TDS profile for $m/z = 32$ and corresponds to the [$^{12}\text{C}^1\text{H}_4^{16}\text{O}$] fragment. Similar to the behavior shown in Fig. S3(b), TDS peaks for the fragments relating to [CH_n] and [CH_nO] were found in the 210–260 °C temperature range, and each fragment exhibited peaks at different temperatures. This is also an indication that residual MeOH decomposes into these fragments at relatively high temperatures, and hence, we tentatively conclude that desorption associated with peaks at 210–260 °C are unlikely to be due to the desorption of water but rather due to the decomposition of molecular MeOH. As this sample was identified to be $\text{Cs}_2[\text{Mo}_6\text{Cl}_{14}] \cdot \text{H}_2\text{O}$, we expected to see a significant

desorption of water molecules. However, the $m/z = 18$ signal intensity for this material was much lower than that observed for the trigonal phase prepared using EtOH.

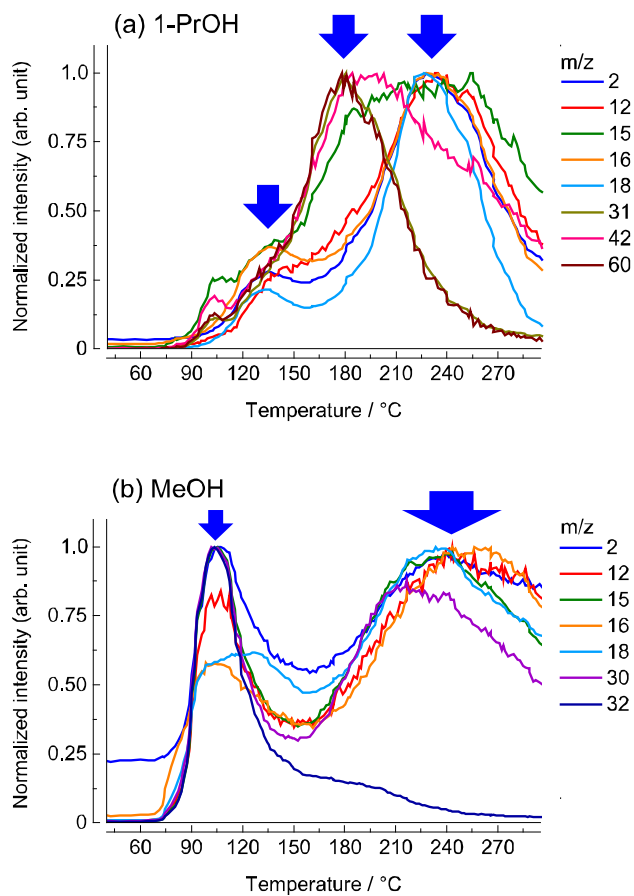


Figure S3 Normalized TDS spectra of (a) trigonal form collected from the 1-PrOH suspension and (b) monoclinic form collected from the MeOH suspension, using $\text{Cs}_2[\text{Mo}_6\text{Cl}_{14}] \cdot \text{H}_2\text{O}$ as precursor. Arrows indicate characteristic desorption peaks.

3.3 FT-IR spectra

Figure S4 shows the FT-IR spectra in the range for C-O and CH_n related modes. The peak at 1601 cm^{-1} may be attributable to the presence of the OH groups of residual alcohol molecules. This assignment is very compatible with the desorption of the $m/z = 18$ fragment observed for the trigonal phase prepared in

1-PrOH, which was not attributed to the desorption of water but mostly to the desorption of residual solvent molecules. In fact, as shown in Fig. S4, several bands corresponding to CH_n and C-O bonds [14] were observed at around 1450 and 1050 cm^{-1} , respectively, in the trigonal phase prepared using EtOH or 1-PrOH, while they were not observed in the sample prepared with MeOH. Hence, it is reasonable to attribute the large desorption peaks observed in the TDS spectra of the trigonal phase to the desorption of residual solvent molecules.

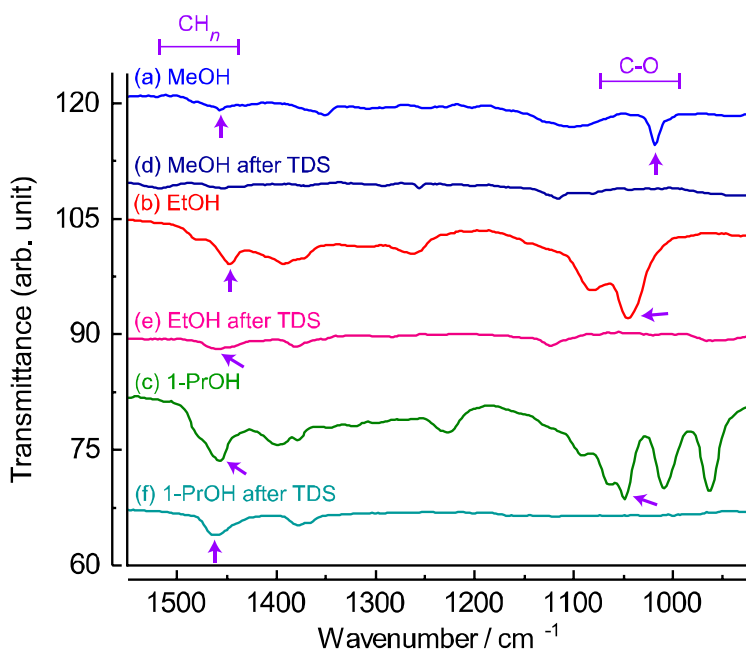


Figure S4 FT-IR spectra of recrystallized samples before and after the TDS measurements. The spectra were obtained by using (a) monoclinic phase crystallized in MeOH, trigonal form crystallized in (b) EtOH or (c) 1-PrOH. The spectra (d)–(f) indicate the sample (a)–(c) heated in vacuum condition through the TDS measurements, respectively. Arrows indicate characteristic peaks associated with the presence of the solvents.

3.4 Lattice parameters of monoclinic phase

Table S3 shows the lattice parameters of the monoclinic phase obtained by the recrystallization experiments using MeOH as solvent. As compared to the lattice parameters of $\text{Cs}_2[\text{Mo}_6\text{Cl}_{14}]\cdot\text{H}_2\text{O}$ presented in Table S2, it is found that the lattice parameters of the monoclinic phase collected from the MeOH suspension were significantly larger irrespective of the precursor phase. This result implies a possibility that MeOH molecule partially substituted to water molecule of $\text{Cs}_2[\text{Mo}_6\text{Cl}_{14}]\cdot\text{H}_2\text{O}$ considering that molecular size of MeOH is comparable to that of water. In other words, the monoclinic phase obtained from the MeOH suspension is attributed to a mixed $\text{H}_2\text{O}/\text{MeOH}$ solvate. While we attempted to refine crystallographic parameters of the recrystallized monoclinic phase by the Rietveld method [15], reliability (R) factor did not converge satisfactorily only by employing the structural model of $\text{Cs}_2[\text{Mo}_6\text{Cl}_{14}]\cdot\text{H}_2\text{O}$. Thus, in the crystal structure of the monoclinic phase, inserted MeOH molecule are probably disordered in room temperature.

Table S3 Refined lattice parameters of the monoclinic phase obtained from the MeOH suspension.

Precursor	Solvent	Lattice parameters
$\text{Cs}_2[\text{Mo}_6\text{Cl}_{14}]$	MeOH	$a = 1.9791(13) \text{ nm}; b = 1.5179(5) \text{ nm}; c = 0.9343(3) \text{ nm};$ $\beta = 115.61(3)^\circ; V = 2.5310(10) \text{ nm}^3$
$\text{Cs}_2[\text{Mo}_6\text{Cl}_{14}]\cdot\text{H}_2\text{O}$	MeOH	$a = 1.9778(30) \text{ nm}; b = 1.5142(8) \text{ nm}; c = 0.9341(4) \text{ nm};$ $\beta = 115.61(5)^\circ; V = 2.5226(31) \text{ nm}^3$

3.5 DFT calculations

The crystal structural parameters are summarized in Table S4. Figure S5 compares projected-densities-of-states (PDOSs). As indicated in Fig. S5, PDOSs of the trigonal and monoclinic phase looked very similar to each other indicating that insertion of water molecule does not affect to the electronic structure of $[\text{Mo}_6\text{Cl}_{14}]^{2-}$ complex. Difference between the monoclinic phase and trigonal phase was found at the energy range from -0.5 to -1.0 eV. That difference was also seen in the band structure exhibited in the main text.

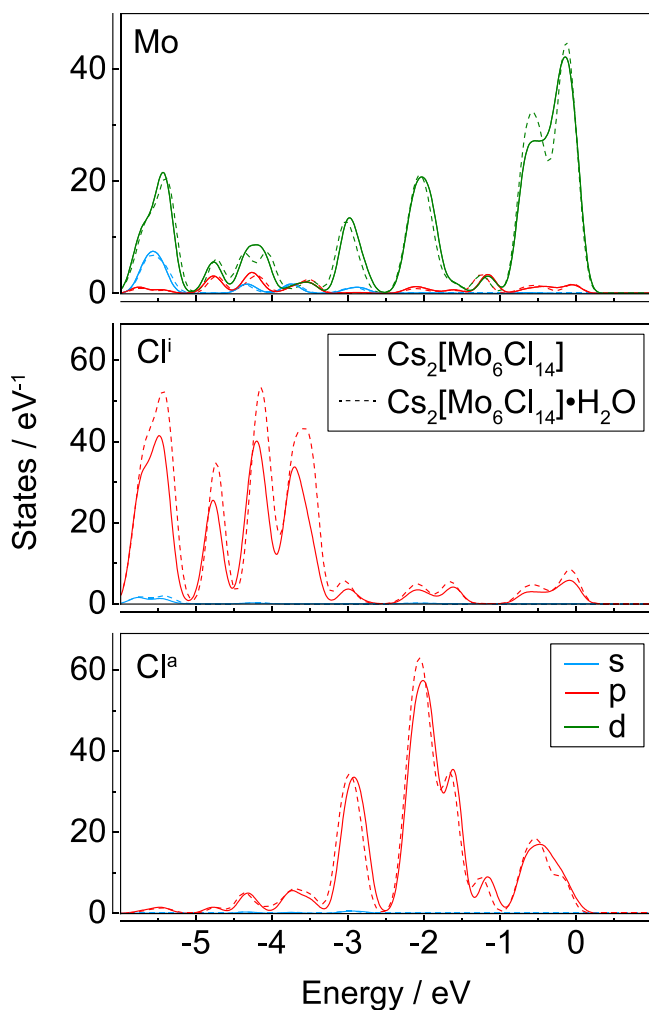


Figure S5 PDOSs of $\text{Cs}_2[\text{Mo}_6\text{Cl}_{14}]$ (solid-line) and $\text{Cs}_2[\text{Mo}_6\text{Cl}_{14}]\cdot\text{H}_2\text{O}$ (break-line).

Table S4 Lattice structure parameters of (a) $\text{Cs}_2[\text{Mo}_6\text{Cl}_{14}]$ and (b) $\text{Cs}_2[\text{Mo}_6\text{Cl}_{14}]\cdot\text{H}_2\text{O}$ optimized by DFT calculation.

(a) $\text{Cs}_2[\text{Mo}_6\text{Cl}_{14}]$

Lattice parameters				
$a = 0.974 \text{ nm}$				
$c = 1.484 \text{ nm}$				
$V = 1.220 \text{ nm}^3$				
Atomic coordinates				
Atom	Sym.	x	y	z
Mo	$12i$	0.666	0.179	0.179
Cl1	$4f$	$2/3$	$1/3$	0.049
Cl2	$12i$	0.956	0.330	0.181
Cl3	$12i$	0.655	-0.037	0.092
Cs1	$2c$	$2/3$	$1/3$	$3/4$
Cs2	$2b$	0	0	0

(b) Cs₂[Mo₆Cl₁₄]•H₂O

Lattice parameters

$a = 1.940 \text{ nm}; b = 1.586 \text{ nm}$

$c = 0.948 \text{ nm}; \beta = 112.2^\circ$

$V = 2.700 \text{ nm}^3$

Atomic coordinates

Atom	Sym.	x	y	z
Mo1	$8f$	0.200	0.265	0.128
Mo2	$8f$	0.301	0.349	0.068
Mo3	$8f$	0.323	0.192	0.151
Cl1	$8f$	0.319	0.303	0.328
Cl2	$8f$	0.182	0.413	0.044
Cl3	$8f$	0.415	0.274	0.087
Cl4	$8f$	0.224	0.117	0.199
Cl5	$8f$	0.131	0.282	0.294
Cl6	$8f$	0.367	0.479	0.151
Cl7	$8f$	0.419	0.112	0.350
Cs1	$4a$	0	0	0
Cs2	$4e$	0	0.436	1/4
O	$4e$	0	0.142	1/4
H	$8f$	0.043	0.180	0.269

REFERENCE

- [1] N. Saito, P. Lemoine, N. Dumait, M. Amela-Cortes, S. Paofai, T. Roisnel, V. Nassif, F. Grasset, N. Ohashi, S. Cordier, From $\text{Cs}_2\text{Mo}_6\text{Cl}_{14}$ to $\text{Cs}_2\text{Mo}_6\text{Cl}_{14}\cdot\text{H}_2\text{O}$ and Vice Versa: Crystal Chemistry Investigations., *J. Clust. Sci.*, 2017, **28**, 773–798.
- [2] M. Potel, C. Perrin, A. Perrin, M. Sergent, New Families of Ternary Molybdenum (II) Chlorides with Octahedral Mo_6 Clusters., *Mat. Res. Bull.*, 1986, **21**, 1239–1245.
- [3] F. W. Koknat, T. J. Adaway, S. I. Erzerum, S. Syed, Convenient Synthesis of the Hexanuclear Molybdenum(II) Halides $\text{Mo}_6\text{Cl}_{12}$ and $\text{Mo}_6\text{Br}_{12}\cdot 2\text{H}_2\text{O}$., *Inorg. Nucl. Chem. Lett.*, 1980, **16**, 307–310.
- [4] N. Saito, S. Cordier, P. Lemoine, T. Ohsawa, Y. Wada, F. Grasset, J. S. Cross, N. Ohashi, Lattice and Valence Electronic Structures of Crystalline Octahedral Molybdenum Halide Clusters-Based Compounds, $\text{Cs}_2[\text{Mo}_6\text{X}_{14}]$ ($\text{X} = \text{Cl}, \text{Br}, \text{I}$), Studied by Density Functional Theory Calculations., *Inorg. Chem.*, 2017, **56**, 6234–6243.
- [5] S. J. Clark, M. D. Segall, C. J. Pickard, P. J. Hasnip, M. J. Probert, K. Refson, M. C. Payne, First Principles Methods Using CASTEP., *Z. Kristallogr.*, 2005, **220**, 567–570.
- [6] A. W. Rappe, K. M. Rabe, E. Kaxiras, J. D. Joannopoulos, Optimized Pseudopotentials., *Phys. Rev. B*, 1990, **41**, 1227–1230.
- [7] D. R. Hamann, M. Schlüter, C. Chiang, Norm-Conserving Pseudopotentials., *Phys. Rev. Lett.*, 1979, **43**, 1494–1497.
- [8] D. R. Hamann, Generalized Norm-Conserving Pseudopotentials., *Phys. Rev. B*, 1989, **40**, 2980–2987.
- [9] D. D. Koelling, B. N. Harmon, A Technique for Relativistic Spin-Polarised Calculations., *J. Phys. C: Solid State Phys.*, 1977, **10**, 3107–3114.
- [10] J. P. Perdew, A. Ruzsinszky, L. G. I. Csonka, O. A. Vydrov, G. E. Scuseria, L. A. Constantin, X. Zhou, K. Burke, Restoring the Density-Gradient Expansion for Exchange in Solids and Surfaces., *Phys. Rev. Lett.*, 2008, **100**, 136406-1–4.

- [11] H. J. Monkhorst, J. D. Pack, Special Points for Brillouin-Zone Integrations., *Phys. Rev. B*, 1976, **13**, 5188–5192.
- [12] J. D. Pack, H. J. Monkhorst, "Special Points for Brillouin-Zone Integrations"—A Reply., *Phys. Rev. B*, 1977, **15**, 1748–1749.
- [13] M. S. B. Munson, F. H. Field, Chemical Ionization Mass Spectrometry. I. General Introduction., *Phys. Inorg. Chem.*, 1966, **88**, 2621–2630.
- [14] E. K. Plyler, Infrared Spectra of Methanol, Ethanol, and n-Propanol., *J. Res. Natl. Bur. Stand.*, 1952, **48**, 281–286.
- [15] H. M. Rietveld, A Profile Refinement Method for Nuclear and Magnetic Structures, *J. Appl. Crystallogr.*, 1969, **2**, 65–71.